Inorganic Chemistry
Article
pubs.acs.org/IC

Rich Crystal Chemistry and Magnetism of “114” Stoichiometric $LnBaFe_4O_{7.0}$ Ferrites

V. Duffort,[†] V. Caignaert,*[,†] V. Pralong,[†] A. Cervellino,[‡] D. Sheptyakov,[§] and B. Raveau[†]

[†]Laboratoire de Cristallographie et Sciences des Matériaux (CRISMAT), Unité Mixte de Recherche 6508, Centre Nationale de la Recherche Scientifique (CNRS)−École Nationale Supérieure d’Ingénieurs de Caen (ENSICAEN), 6 Boulevard du Maréchal Juin, FR-14050 Caen, France

[‡]Material Science Beamline, SLS, and [§]Laboratory for Neutron Scattering, Paul Scherrer Institut, CH-5232 Villigen PSI, Switzerland

ABSTRACT: Stoichiometric $LnBaFe_4O_{7.0}$ oxides with Ln = Dy to Lu have been synthesized and protected in order to prevent oxidation at room temperature. The structural study of these compounds, using laboratory and synchrotron X-ray as well as neutron powder diffraction, shows the extraordinary flexibility of the tetrahedral $[Fe_4]$ sublattice of these compounds, which exhibit various distortions. At room temperature they all are tetragonal ($I\bar{4}$), and at higher temperature ($T > 580$ K) they exhibit a cubic symmetry ($F\bar{4}3m$). Moreover, the low-temperature structures of these oxides are dependent on the nature of the Ln^{3+} cation. At 110 K, compounds with Ln = Dy and Ho adopt the same monoclinic ($P12_11$) structure as $YBaFe_4O_{7.0}$, whereas $YbBaFe_4O_{7.0}$ possesses a new centered monoclinic cell ($I121$), and members with Ln = Er and Lu keep the tetragonal ($I\bar{4}$) symmetry. Neutron diffraction patterns evidence long-range magnetic ordering only for the most distorted structures (Ln = Dy and Ho), showing that the geometric frustration generated by the tetrahedral $[Fe_4]_\infty$ sublattice can be lifted only with the most severe distortions. The other oxides (Ln = Er, Yb, and Lu) with weakly distorted $[Fe_4]_\infty$ sublattices do not exhibit magnetic ordering down to 4 K, demonstrating the importance of magnetic frustration. The behavior of these “114” iron oxides is compared to the cobalt family, showing in both cases a striking underbonding of barium.

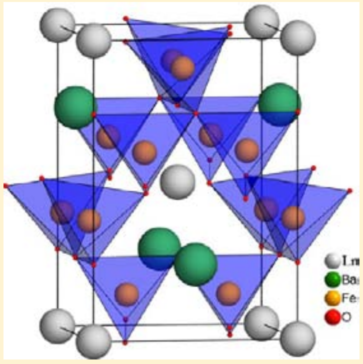

INTRODUCTION

The discovery of the oxide $YBaCo_4O_7$[1,2] has opened a route to exploration of a new series of strongly electron-correlated oxides with the generic formula $LnBaCo_4O_7$, which were extensively studied by many groups for their complex magnetic properties and especially for their ability to exhibit competition between one-dimensional magnetic ordering and two-dimensional (2D) magnetic frustration.[3−9] Among this family, denoted “114”, another member, $CaBaCo_4O_7$, was more recently found to be ferrimagnetic and to exhibit multiferroic properties.[10−12] The exceptional magnetic properties of these mixed-valent oxides, Co(II)−Co(III), originates from their particular structure built up of two sorts of layers of CoO_4 tetrahedra, kagomé and triangular. The stacking of undistorted planes leads to a hexagonal structure that confers a triangular geometry to the cobalt sublattice. As a result, the geometric frustration that takes place for a hexagonal structure can be possibly lifted by structural distortions versus temperature, depending on the size of the Ln^{3+}/Ca^{2+} cations.[3,4,7,10,11,13,14] Moreover the diversity of properties of these oxides is enriched by their ability to absorb oxygen, leading to oxides $LnBaCo_4O_{7+\delta}$[15−18] and $CaBaCo_4O_{7+\delta}$[19] with very closely related structures.

The great potential of iron for the generation of new “114” oxides with mixed-valent Fe(II)−Fe(III) was later demonstrated by the synthesis of ferrimagnetic oxides $CaBaFe_4O_{7+\delta}$ and $LnBaFe_4O_{7+\delta}$ with Ln = Tb, Gd ($\delta > 0$)[20,21] and of the spin-glass-like $LnBaFe_4O_{7+\delta}$ ($\delta > 0$) oxides, with Ln = Y and Lu to Dy.[21−24] The ferrimagnetic compounds were shown to exhibit a hexagonal structure at room temperature, similar to the cobaltites, whereas for the second series a cubic structure, closely related to the hexagonal form, was observed. Importantly, the possibility of oxygen hyperstoichiometry in these oxides was demonstrated, showing that the room-temperature stoichiometric form of $YBaFe_4O_{7.0}$ is in fact tetragonal and is rapidly oxidized in air at room temperature into the cubic form $YBaFe_4O_{7+\delta}$, with δ values between 0 and 0.8, depending on the exposure time to air.[23] In a recent study of the stoichiometric ferrite $YBaFe_4O_{7.0}$,[24] we have shown that, besides the tetragonal room-temperature (RT) and the cubic high-temperature (HT) forms, there exists a low-temperature monoclinic (LT) form below 190 K, which is antiferromagnetic with a Néel temperature $T_N = 95$ K. In the present study, we have extended our investigations to the stoichiometric oxides $LnBaFe_4O_{7.0}$, with Ln = Dy to Lu, that are isostructural with $YBaFe_4O_{7.0}$. Controlling carefully the “O_7” stoichiometry during synthesis and structural characterizations, we show that the properties of these oxides are strongly dependent on the nature of the lanthanide.

EXPERIMENTAL SECTION

Synthesis of Stoichiometric Oxides $LnBaFe_4O_{7.0}$. Similarly to $YBaFe_4O_{7.0}$, the stoichiometric oxides $LnBaFe_4O_{7.0}$ can be synthesized by two methods, either in sealed tubes or in hydrogenated argon flow.

Received: May 21, 2013
Published: August 29, 2013

In the first method, the precursors Ln_2O_3 (Ln = Dy, Ho, Er, Tm, Yb, Lu), $BaFe_2O_4$, Fe_2O_3, and Fe are intimately mixed in stoichiometric proportions and pressed in the form of parallelepipedic bars under 200 MPa. The bars are placed in alumina fingers and heated in quartz tubes sealed under vacuum (5×10^{-3} atm), up to 1100 °C in 6 h, maintained at this temperature for 24 h, and finally quenched to room temperature. The sealed tubes must be opened in the glovebox in order to avoid oxidation in air.

The second method is realized by dissolving Ln_2O_3, $BaCO_3$, and $Fe(C_2O_4)\cdot H_2O$ in melted citric acid and calcining the so-obtained citrate gel. The ashes are pressed in the form of parallelepipedic bars and heated slowly in an Ar/H_2 1% atmosphere, humidified by bubbling in 16 °C distilled water, up to 900 °C and maintained at this temperature for 6 h in order to achieve a complete decarbonation. In a second step, the temperature is increased at 1 °C/min up to 1050 °C, maintained at this temperature for 24 h, and finally cooled slowly (1 °C/min) down to room temperature. This second method has the advantage of allowing additional annealing in case of incomplete reaction, but in contrast to the sealed tube method, it does not allow the stoichiometric phase to be obtained directly, since the products are exposed to air before transfer to the glovebox, leading to the cubic phases $LnBaFe_4O_{7+\delta}$.[21] Then an additional annealing is carried out at 500 °C under Ar/H_2 (5%) atmosphere during 12 h, in an airtight alumina tube, allowing the transfer of stoichiometric $LnBaFe_4O_{7.0}$ in the glovebox without any oxidation.

Chemical Analysis. Determination of the oxygen content is carried out by cerimetric titration of Fe^{2+} in argon atmosphere in order to avoid partial oxidation by dissolved oxygen in the solution. To protect the sample from oxidation before titration, the latter was weighed and encapsulated in a gelatin cell in the glovebox, and an airtight glass bottle was used for the transfer, as previously described for $YBaFe_4O_{7.0}$.[23]

X-ray Powder Diffraction, Synchrotron, and Neutron Powder Diffraction. For room- and low-temperature studies, synchrotron and neutron powder diffraction (NPD) techniques were used, as described for $YBaFe_4O_{7.0}$.[23] For the NPD study, the sample was placed in a vanadium can inside the glovebox and sealed by pressing an indium wire in between two flanges of the holder. The NPD data were registered with the high-resolution HRPT diffractometer of the Paul Scherrer Institute (Villigen) at 300 and 110 K with $\lambda = 1.494$ Å and at 4 K with $\lambda = 1.886$ Å.

For the synchrotron study, the sample was placed in a glass capillary tube, corked with vacuum grease inside the glovebox. The capillary was then removed out of the glovebox and rapidly sealed by flame-fusion. The synchrotron X-ray powder diffraction (SXPD) experiments were performed on the X04SA beamline of the Swiss Light Source (SLS) of the Paul Scherrer Institute with calibrated wavelength $\lambda = 0.616\,611$ Å (20 keV), using the Mythen 1D detector.

For high-temperature studies, the thermodiffraction patterns were registered with a chamber Anton Paar HTK1200, mounted on a Bragg–Brentano θ-2θ D8 Advance Bruker diffractometer using Cu Kα1 radiation ($\lambda = 1.540$ 59 Å). The diffracted intensity was measured with a Lynx Eye detector, with a limited spectral range in order to minimize the background noise due to iron fluorescence. The patterns were registered in the 2θ range 10–90° in order to avoid any fall of the powder from the diffractometer. These measurements were carried out starting from the air-exposed $LnBaFe_4O_{7+\delta}$ samples, heated in the thermodiffraction chamber under He/H_2 (5%) flow up to 500 °C in order to ascertain the $LnBaFe_4O_{7.0}$ stoichiometry for all temperatures in the range 500–30 °C.

Differential Scanning Calorimetry. Differential scanning calorimetry (DSC) analyses were performed on a DSC2920 from TA Instruments with speed 10 K/min between 110 and 300 K. The powdered sample was loaded in an airtight aluminum crucible, which was sealed by pressing the flange of the upper and lower part inside the glovebox. The aluminum capsule was rapidly transferred from the glovebox to the DSC apparatus.

■ RESULTS AND DISCUSSION

Room-Temperature Tetragonal and High-Temperature Cubic Forms of $LnBaFe_4O_{7.0}$ Oxides. All the stoichiometric $LnBaFe_4O_{7.0}$ oxides of the series Ln = Dy, Ho, Er, Tm, Yb and Lu exhibit, like $YBaFe_4O_{7.0}$,[23] a structural transition from a cubic (C) cell at 773 K to a tetragonal cell (T) at room temperature. As exemplified from the diffraction patterns of $HoBaFe_4O_{7.0}$ (Figure 1), the RT form corresponds to a tetragonal distortion of the HT (773 K) cubic form, with $a_T \approx a_C/\sqrt{2} = 6.4$ Å and $c_T \approx c_C \approx 9.1$ Å.

The evolution of the cell parameters of these two forms versus the ionic radius of Ln^{3+}, at 773 K (Figure 2a) and at 300 K (Figure 2b), shows that a_C as well as a_T and c_T increase practically in a linear manner as $r_{Ln^{3+}}$ increases. The amplitude of the tetragonal distortion can be deduced from the ratio $\rho = a_T\sqrt{2}/c_T$, which deviates from unity with respect to the cubic form. This value, systematically smaller than 1, corresponds to an expansion of the cubic cell along one direction (c_T) and to a contraction along two other directions (a_T). Quite remarkably, one observes that ρ gets closer to 1 as the size of Ln^{3+} decreases from Dy^{3+} ($\rho \sim 0.970$), reaching the weaker distortion ($\rho \sim 0.983$) for Lu^{3+}.

Refinement of the crystal structure parameters of HT cubic forms of the $LnBaFe_4O_{7.0}$ series, carried out from thermodiffraction patterns registered at 773 K, could only be carried out on a limited number of reflections, that is, 26 reflections, due to the narrow 2θ range (10–90°) studied. Thus, the accuracy of determination of the atomic coordinates (Figure 3) and of the interatomic distances (Table 1) must be considered as limited. Nevertheless, when the ideal cubic structure is considered (Figure 4), which would consist of regular FeO_4 tetrahedra and LnO_6 octahedra with identical O–O distances, corresponding to ideal coordinates $x_{Fe} = 0.375$ and $x_{O1} = 0.75$, some conclusions can be drawn. First, the positions x_{Fe} and x_{O1} are not significantly dependent on the nature of the Ln^{3+} cations (Figure 3) and remain close to the ideal values, suggesting that minimization of strain is mainly ensured by variation of the cell parameters. Second, the FeO_4 tetrahedra show a significant elongation of the Fe–O2 bond (>2 Å), whereas the three equivalent Fe–O1 bonds are systematically shorter (<2 Å) (Table 1). Third, the Ba–O distances, ranging from 3.19 to 3.16 Å, imply a strong underbonding of barium, whose calculated valence according to bond valence sum (BVS)[25] is much smaller than 2, that is, ~1.1. This large discrepancy points out that the basic parametrization of the BVS formalism is inappropriate for this class of oxides due to the important strain in the structure.[26,27] Therefore, BVS calculations are used here only as an indicator of the mean bond length.

Such an underbonding of barium, previously observed for $LnBaCo_4O_7$ cobaltites[3,8,10] and $YBaFe_4O_{7.0}$,[23] most probably affects strongly the positions of the O1 atoms, which should exhibit an anisotropic thermal displacement directed toward the Ba site as reported for cobalt- and iron-based 114 oxides. The latter cannot be proved here, due to the quality of the data registered at 773 K. Nevertheless, it appears clearly that O1 atoms, which form the LnO_6 octahedra and are simultaneously affected by the barium underbonding, play a crucial role in the structural transition from the HT cubic form to the RT tetragonal phase that takes place in this system.

The RT structures of tetragonal $LnBaFe_4O_{7.0}$ oxides with Ln = Dy, Ho, and Lu were solved from synchrotron and neutron data. Those of Ln = Er and Yb were refined from neutron patterns only. The structure of $TmBaFe_4O_{7.0}$ was not investigated, due to the high cost of this compound. The cell parameters of this oxide were determined only from X-ray powder diffraction data and consequently will not be discussed here due to their lower accuracy compared to synchrotron and NPD data obtained for other oxides. Refinement of the structural parameters of these oxides was carried out in the same way as for tetragonal $YBaFe_4O_{7.0}$,[23] using FullProf software[28] to refine synchrotron and neutron patterns simultaneously, assigning equivalent weight to both patterns. As for $YBaFe_4O_{7.0}$, the Rietveld refinements were performed in the space group $I\bar{4}$, leading to

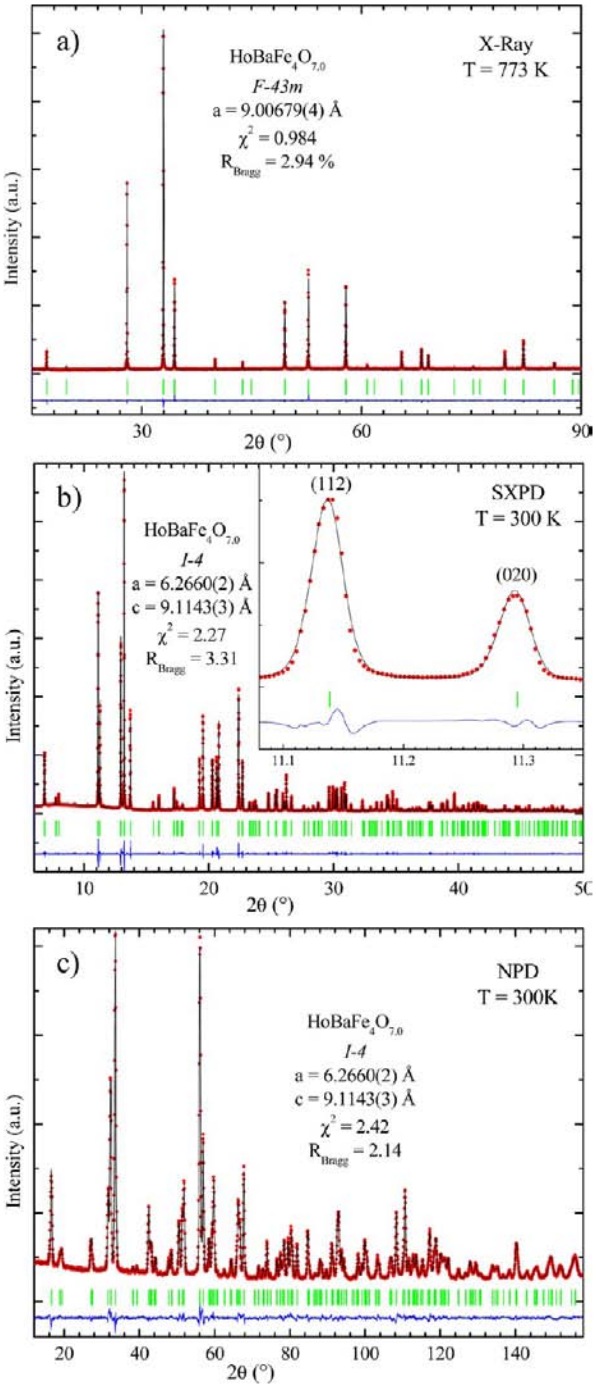

Figure 1. Rietveld fitting of the patterns of HoBaFe$_4$O$_{7.0}$: (a) at 773 K by X-ray thermodiffraction (λ = 1.540 59 Å), (b) at 300 K by synchrotron radiation (λ = 0.616 611 Å), and (c) at 300 K by neutron diffraction (λ = 1.494 Å).

quite satisfactory agreement factors; the good agreement between experimental and calculated synchrotron and neutron patterns is exemplified for HoBaFe$_4$O$_{7.0}$ in Figure 1b,c. The rather high χ^2 values are due to strong microstructural effects (Table 2). One observes, as for YBaFe$_4$O$_{7.0}$, *hkl*-dependent asymmetric profile originating from the microstructure, in particular because of twinning due to the loss of rotational symmetry element. The atomic coordinates and anisotropic displacement parameters (Table A1 in the Appendix) are very similar to those of tetragonal YBaFe$_4$O$_{7.0}$.[23] The structure of all compounds of the series (Figure 5) is then closely related to the cubic form and can be described mainly by the combination of two distortion modes, GM1 and GM5 (Table 2), which were calculated from the Amplimode program.[29] Atomic displacements with respect to the cubic structure corresponding to these modes are shown by arrows in Figure 5b,c.

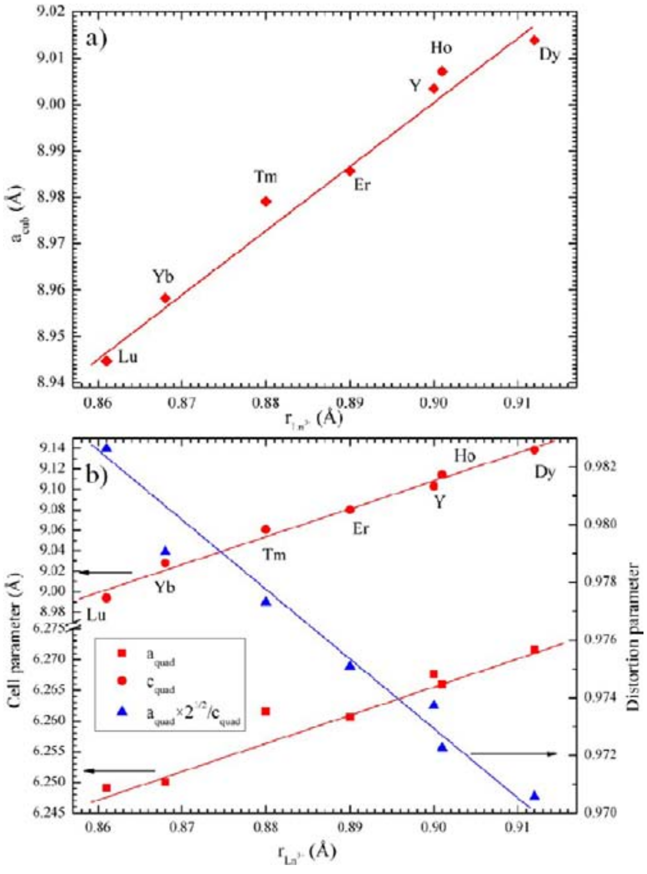

Figure 2. Evolution of cell parameters of LnBaFe$_4$O$_{7.0}$ (Ln = Y, Dy to Lu) vs ionic radius of Ln^{3+} for (a) cubic structure at 773 K and (b) tetragonal structure at 300 K.

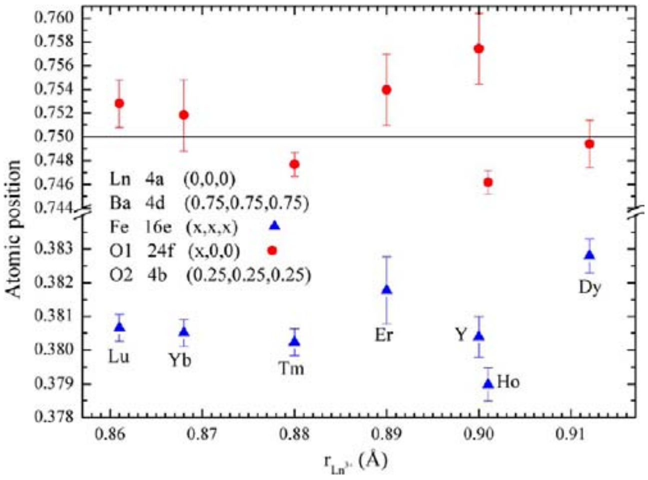

Figure 3. Atomic positions of the cubic structure of LnBaFe$_4$O$_{7.0}$, with Ln = Y and Dy to Lu, as extracted from Rietveld refinement of their X-ray thermodiffraction patterns at 773 K.

The amplitude of the GM1 mode, that is, the degrees of freedom compliant with the HT symmetry, which allows it to accommodate the strains during thermal contraction of the cell parameters, increases

Table 1. Interatomic Distances in the Cubic Form of $LnBaFe_4O_{7.0}$ (Ln = Dy to Lu) at 773 K

	Dy	Ho	Er	Tm	Yb	Lu
Ln−O (Å)	2.26(2) × 6	2.29(1) × 6	2.21(2) × 6	2.27(1) × 6	2.22(3) × 6	2.21(1) × 6
Ba−O (Å)	3.19(1) × 12	3.185(6) × 12	3.18(1) × 12	3.175(3) × 12	3.167(6) × 12	3.163(8) × 12
Fe−O (Å)	1.91(1) × 3	1.91(1) × 3	1.94(2) × 3	1.91(1) × 3	1.92(1) × 3	1.92(1) × 3
	2.09(1) × 1	2.01(1) × 1	2.05(1) × 1	2.03(1) × 1	2.03(1) × 1	2.02(1) × 1

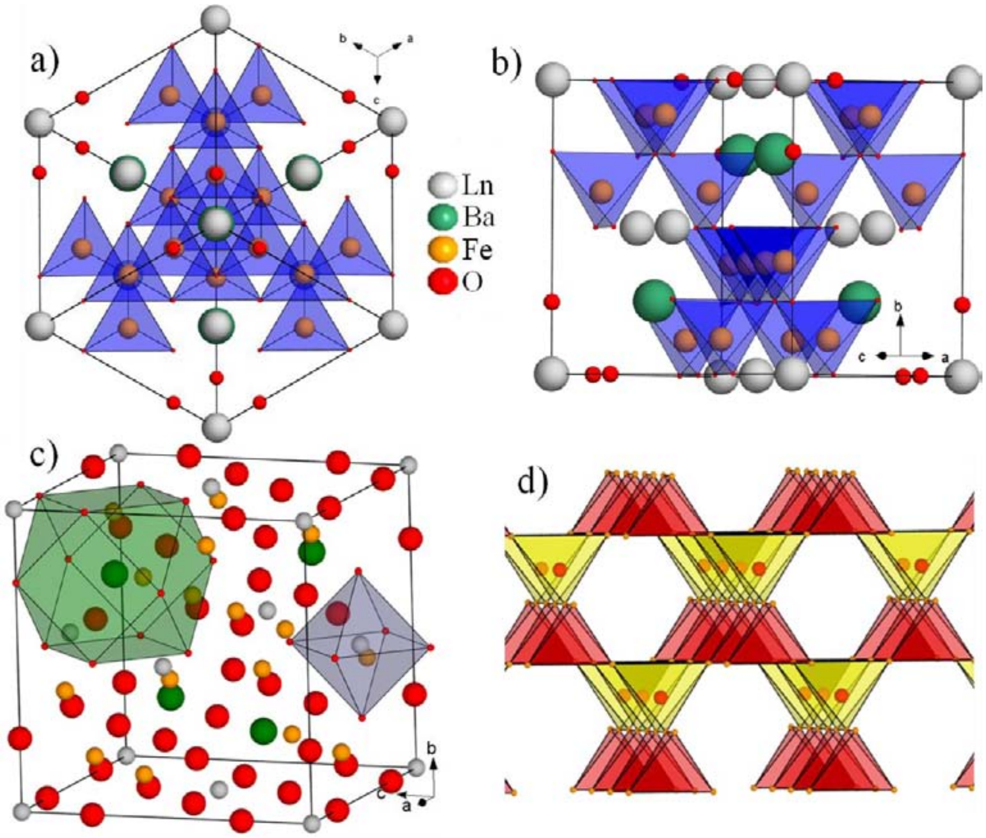

Figure 4. Representation of ideal cubic structure of $LnBaFe_4O_{7.0}$: (a) view along the [111] direction, (b) view along the [110] direction, (c) visualization of LnO_6 and BaO_{12} coordination polyhedral, and (d) visualization of the Fe_∞ framework composed of vertex-sharing Fe_4 (red) and Fe_4O (yellow) tetrahedra.

Table 2. Details of Rietveld Refinements of Tetragonal Patterns of $LnBaFe_4O_{7.0}$ (Ln = Dy to Lu) at 300 K

	Dy[a]	Ho[a]	Er[b]	Tm[c]	Yb[b]	Lu[a]
χ^2 (SXPD)	2.2	2.27				2.72
R_{Bragg} (SXPD)	3.01	3.31				2.68
χ^2 (NPD)	2.41	2.42	1.83		1.42	2.07
R_{Bragg} (NPD)	3.19	2.14	2.15		1.61	2.08
a_{quad} (Å)	6.2717(3)	6.2660(2)	6.2606(2)	6.2615(1)	6.2500(1)	6.2491(3)
c_{quad} (Å)	9.1383(3)	9.1143(3)	9.0801(3)	9.0607(2)	9.0279(2)	8.9938(6)
amplitude GM1 (Å)	0.452(8)	0.484(6)	0.508(8)	0.42(5)	0.534(6)	0.546(8)
amplitude GM5 (Å)	0.94(1)	0.905(8)	0.856(8)	0.92(6)	0.802(8)	0.728(8)
BVS (Ln)	2.91	3.23	3.35	2.64	3.55	3.63
BVS (Ba)	1.51	1.49	1.44	1.62	1.41	1.35
BVS (Fe)	2.17	2.18	2.18	2.32	2.20	2.23

[a] Synchrotron radiation. [b] Neutron diffraction. [c] Thermodiffraction.

linearly as the size of Ln^{3+} decreases (Table 2). This corroborates the mechanism previously proposed for $YBaFe_4O_{7.0}$.[23] As the size of Ln^{3+} decreases, the cell parameters decrease and consequently the coulombic repulsion that governs GM1 mode increases. It results in large atomic displacements for all the compounds, keeping the Fe−O bonds homogeneous (Table 3) with a rather constant average distance ranging from 1.96 Å in $DyBaFe_4O_{7.0}$ to 1.95 Å in $LuBaFe_4O_{7.0}$.

The amplitude of the GM5 mode follows reverse evolution (Table 2): it decreases with Ln^{3+} size, similar to the amplitude of tetragonal distortion of the cell (Figure 2b). This weaker distortion of the cell for smaller Ln^{3+} cations cannot be explained

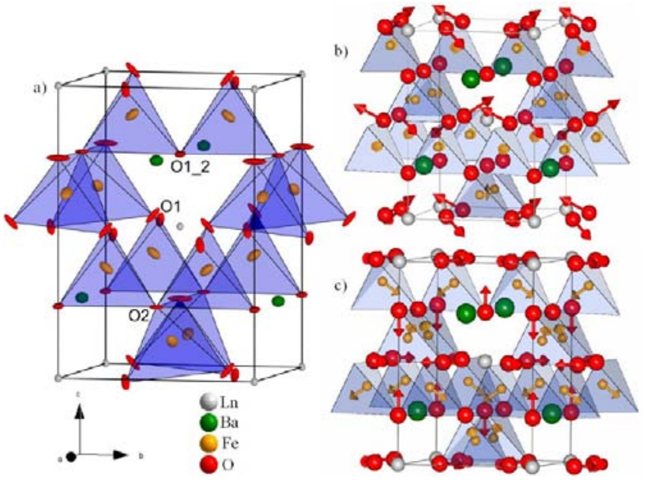

Figure 5. Representation of tetragonal structure adopted by the $LnBaFe_4O_{7.0}$ series at room temperature (atomic position of Ln = Ho): (a) view of thermal vibration ellipsoids, (b) atomic shifts of the primary mode GM5 for cubic to tetragonal distortion, and (c) atomic shifts of the GM1 mode for cubic to tetragonal distortion.

by smaller Ba−O distances (Table 3), since the opposite is observed, that is, d(Ba−O) increases from 2.76 Å for Dy to 2.82 Å for Lu. This weaker distortion of the structure of the $LnBaFe_4O_{7.0}$ oxides with smaller lanthanides is to date not explained. It appears that an internal strength is in opposition to the tetragonal distortion, probably related to the strains that are developed in this structure, in connection with the particular underbonding of barium.

The orientation of the anisotropic thermal atomic displacements (Table A2 in the Appendix) does not vary significantly in the whole series. This is especially the case of the oxygen atoms forming the LnO_6 octahedra (O1 and O1_2), which are all directed toward the Ba positions (Figure 5a) as a result of the large barium underbonding. The strong anisotropic displacement parameters that are required to fit the diffraction patterns could be due either to a static displacive disorder (averaging different configuration) or to a dynamical disorder (vibration). The amplitude of the O1 displacements, the only oxygen atom affected by the primary mode (GM5) of the tetragonal distortion, is, however, dependent on the nature of the Ln^{3+} cation; the smaller the rare earth cation, the larger the thermal displacements of O1. As previously described, small Ln^{3+} cations imply a weaker tetragonal distortion resulting in longer Ba−O bonds. Thus this instability is compensated by a larger displacive disorder (or vibration) of the oxygen atoms.

Structural Transitions versus Temperature. Temperatures of the cubic−tetragonal structural transitions T_s were determined by differential scanning calorimetry (DSC). The evolution of the DSC signal versus temperature (Figure 6a) shows that T_s increases with the size of the Ln^{3+} cation, from 530 K for Lu to 600 K for Dy at increasing temperature (T to C symmetry), and decreases from 580 K (Dy) to 510 K (Lu) at decreasing temperature (C to T symmetry). The exothermic nature of the transition from cubic to tetragonal symmetry is in agreement with the entropy decrease due to reduction of the displacive disorder (or shrinking of the vibration amplitudes) of the O1 atoms implied by the structural distortion. The width of the transition, which extends over several tens of degrees, characteristic of a second-order transition, shows that the structure is progressively distorted as the displacive disorder (or the amplitude of the vibrations) decreases. Nevertheless, one also observes a significant hysteresis, suggesting a possible mixture of first- and second-order transitions. This evolution of the transition temperature is easily explained by the strains imposed by the underbonding of barium. Indeed, the required energy for stabilization of the cubic form should increase with Ba−O distance (Table 1), and consequently the transition temperature should increase with the cell parameters. Note that, similarly, a structural transition from hexagonal to orthorhombic symmetry was also observed for the $LnBaCo_4O_7$ oxides,[3−5,9,14] which were also shown to exhibit a similar underbonding of barium. Remarkably, the cobaltites cover a much larger temperature range versus the lanthanide size, that is, from 400 K for $HoBaCo_4O_7$ to 150 K for $LuBaCo_4O_7$.

The low-temperature investigation of structural transitions in the range 4−300 K, carried out previously for $YBaFe_4O_{7.0}$,[24] showed that a second structural transition at T_s' = 180 K was observed, leading to a monoclinic form with space group $P12_11$. The DSC measurements carried out for $LnBaFe_4O_{7.0}$ oxides (Figure 6b) in this temperature range show a clear signal for Ln = Dy and Ho at increasing temperature, similar to $YBaFe_4O_{7.0}$, whereas no signal is detected for Ln = Er, Tm, Yb, and Lu. The signature of this transition is significantly attenuated at decreasing temperature due to experimental restriction. The T_s' values of 187 and 184 K for Ln = Dy and Ho, respectively, exhibit hysteresis of ∼10 K. Thus, the oxides $DyBaFe_4O_{7.0}$ and $HoBaFe_4O_{7.0}$ exhibit, like $YBaFe_4O_{7.0}$, a LT monoclinic form with space group $P12_11$, as will be further described, from their synchrotron and neutron diffraction study. Differently, in agreement with the disappearance of the DSC signal, the oxides $LnBaFe_4O_{7.0.}$ with Ln = Er and Lu do not show any modification of their symmetry inn the synchrotron and neutron diffraction patterns

Table 3. Interatomic Distances in Tetragonal Structure of $LnBaFe_4O_{7.0}$ (Ln = Dy to Lu) at 300 K

Dy[a]	Ho[a]	Er[b]	Tm[c]	Yb[b]	Lu[a]
		Ln−O (Å)			
2.262(6) × 4	2.242(4) × 4	2.235(4) × 4	2.30(2) × 4	2.215(4) × 4	2.215(6) × 4
2.284(4) × 2	2.266(4) × 2	2.253(3) × 2	2.31(2) × 2	2.228(3) × 2	2.226(4) × 2
		Ba−O (Å)			
2.760(6) × 4	2.783(4) × 4	2.785(4) × 4	2.72(3) × 4	2.798(4) × 4	2.823(6) × 4
3.136(1) × 4	3.133(1) × 4	3.130(1) × 1	3.131(1) × 4	3.125(1) × 4	3.125(1) × 4
		Fe−O (Å)			
1.926(4) × 1	1.922(3) × 1	1.923(1) × 1	1.84(3) × 1	1.922(3) × 1	1.914(3) × 1
1.955(6) × 1	1.948(4) × 1	1.937(4) × 1	1.88(2) × 1	1.932(4) × 1	1.927(6) × 1
1.960(6) × 1	1.950(4) × 1	1.962(4) × 1	2.03(3) × 1	1.958(6) × 1	1.939(6) × 1
2.006(2) × 1	2.030(1) × 1	2.019(1) × 1	2.05(1) × 1	2.017(3) × 1	2.017(3) × 1

[a] Synchrotron radiation. [b] Neutron diffraction. [c] Thermodiffraction.

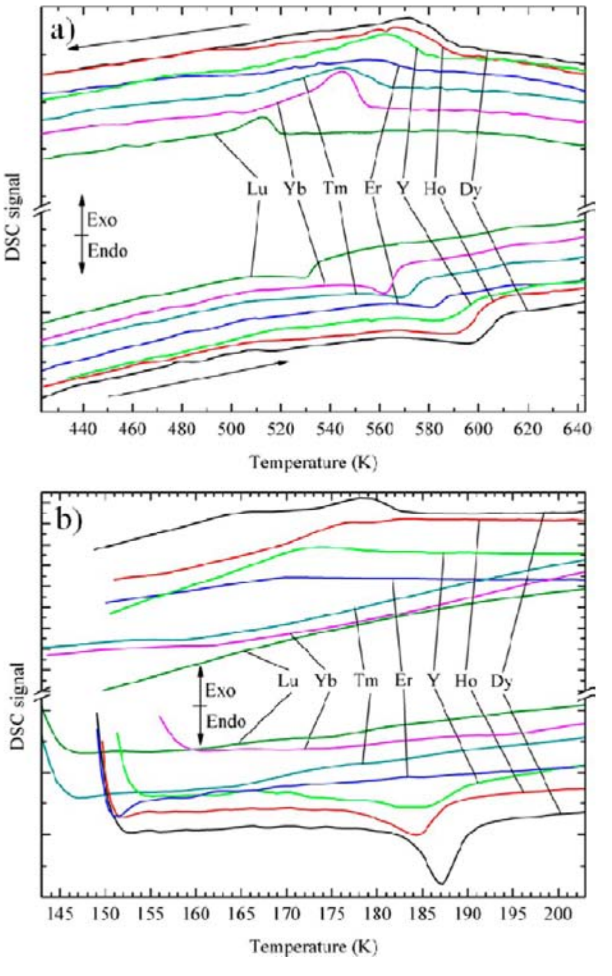

Figure 6. Determination of structural transition temperatures of $LnBaFe_4O_{7.0}$ oxides by DSC: (a) cubic to tetragonal transition and (b) tetragonal to monoclinic distortion.

Table 4. Details of Rietveld Refinement of Monoclinic Patterns of $LnBaFe_4O_{7.0}$ (Ln = Dy and Ho) at 110 K

	$DyBaFe_4O_{7.0}$	$HoBaFe_4O_{7.0}$
χ^2 (SXPD)	3.68	3.80
R_{Bragg} (SXPD)	4.27	4.41
χ^2 (NPD)	2.4	3.59
R_{Bragg} (NPD)	3.5	3.22
a_{mono} (Å)	6.2843(6)	6.2743(6)
b_{mono} (Å)	9.1480(6)	9.1333(6)
c_{mono} (Å)	6.2125(6)	6.2080(6)
β (deg)	89.606(1)	89.6155(9)
amplitude GM1 (Å)	0.15(1)	0.23(2)
amplitude GM4 (Å)	0.24(3)	0.17(3)
amplitude GM5 (Å)	1.37(3)	1.39(3)
amplitude X5 (Å)	0.54(3)	0.51(3)

versus temperature, remaining tetragonal in the whole temperature range from room temperature to 4 K. Finally, the particular behavior of the oxide $YbBaFe_4O_{7.0}$ must be emphasized. Though it does not show any signature of a structural transition on the DSC scans, this phase exhibits a slight monoclinic distortion in the range 4−110 K visible in its NPD patterns. It will be shown further that the structure of this oxide, though monoclinic, is different from the other monoclinic oxides, showing a different space group, $I121$.

Nuclear and Magnetic Structures of Monoclinic $LnBaFe_4O_{7.0}$ Oxides with Ln = Dy and Ho. The NPD and SXPD patterns of these monoclinic oxides registered at 110 K are very similar to those previously observed for $YBaFe_4O_{7.0}$, showing the $P12_11$ space group with $a_M \approx a_T$, $b_M \approx c_T$, $c_M \approx a_T$ and $\beta \approx 90°$ (Table 4). The χ^2 values are strongly affected by microstructural effects as previously observed for $YBaFe_4O_{7.0}$.[24] Moreover, the limited number of data in regard to the large number of variable parameters does not allow anisotropic thermal factors to be refined from powder data. The atomic coordinates of these two phases (Table A3 in the Appendix) are very close to those reported previously for $YBaFe_4O_{7.0}$.[24] Similarly to $YBaFe_4O_{7.0}$, this monoclinic distortion of the tetragonal cell is weak, compared to the tetragonal distortion of the cubic cell. Indeed, GM5, the primary mode of the tetragonal distortion has a high amplitude (1.37−1.39 Å), whereas the monoclinic distortion, corresponding to GM4 and X5 modes, is much weaker (Table 4). Atomic shifts of the monoclinic structure with respect to the tetragonal symmetry are shown by arrows in Figure 7 for $HoBaFe_4O_{7.0}$. These atomic displacements correspond to the shifts allowed by lowering of the symmetry from the tetragonal $I\bar{4}$ group to the monoclinic $P12_11$ group. One observes that the position of the Ln^{3+} cation is fixed, and that among these complex displacements, all the oxygen atoms O1 are displaced toward one barium atom, whereas the barium atoms are displaced along $\vec{a}$ toward one oxygen atom. This definitively shows that this tetragonal to monoclinic transition is, like for the Y-phase, governed by the underbonding of barium. The interatomic distances (Table 5) show that the LnO_6 octahedra, though significantly more distorted than in the tetragonal phase (Table 3), exhibit a close average Ln−O distance. From the Fe−O distances, one observes that two FeO_4 tetrahedra, labeled Fe1 and Fe2, are less distorted and exhibit a smaller size than the two others, labeled Fe3 and Fe4 (Table 5). Note also that the Fe3 and Fe4 tetrahedra are significantly more distorted than in the tetragonal phase (Table 3). The shortest Ba−O distance is close to 2.7 Å, as in the monoclinic Y-phase. It leads to a similar calculated barium valence of 1.61 (instead of 1.63 in $YBaFe_4O_{7.0}$), showing that the barium cation is still underbonded in these monoclinic phases.

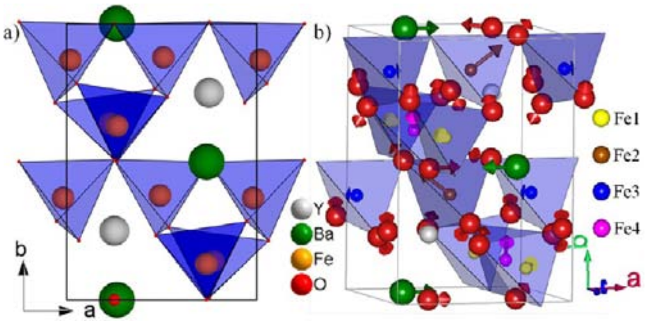

Figure 7. Visualization of monoclinic structure adopted at low temperature by the oxides $LnBaFe_4O_{7.0}$ with Ln = Y, Dy, and Ho: (a) structure and (b) atomic shifts due to monoclinic distortion.

The NPD patterns of $DyBaFe_4O_{7.0}$ and $HoBaFe_4O_{7.0}$ registered at 4 K (Figure 8), very similar to that of $YBaFe_4O_{7.0}$, exhibit two series of magnetic reflections: a set of intense peaks, with a propagation vector $\mathbf{k}_1 = (0, 0, {}^1/_2)$, and a set of very weak peaks, with an incommensurate propagation vector $\mathbf{k}_2 = ({}^1/_3 + \varepsilon, 0, {}^1/_2)$, with $\varepsilon = 0.049$ and 0.012 for Ln = Dy and Ho, respectively. This second set of reflections could originate from the tripling of the magnetic cell ($\mathbf{k}_1$), but their intensity is too

Table 5. Interatomic Distances in Monoclinic Structure of $LnBaFe_4O_{7.0}$ (Ln = Ho and Dy) at 110 K

	$DyBaFe_4O_{7.0}$	$HoBaFe_4O_{7.0}$
Ln−O	2.19(3)−2.23(3)−2.28(3) 2.28(3)−2.32(3)−2.34(3)	2.20(2)−2.22(2)−2.24(2) 2.26(2)−2.26(2)−2.29(2)
Ba−O	2.69(3)−2.74(3)−2.77(3)−2.77(3) 2.90(3)−2.94(3)−3.27(3)−3.39(3)	2.69(2)−2.71(2)−2.75(3)−2.79(2) 2.91(2)−2.99(2)−3.22(2)−3.36(2)
Fe1−O	1.87(3)−1.94(4)−1.97(3)−1.98(3)	1.91(2)−1.91(3)−1.99(2)−2.00(2)
Fe2−O	1.89(3)−1.92(4)−1.95(3)−1.98(3)	1.92(2)−1.94(2)−1.97(3)−1.98(2)
Fe3−O	1.91(4)−1.98(3)−2.05(3)−2.10(3)	1.95(2)−1.97(2)−1.98(2)−2.06(3)
Fe4−O	1.90(3)−1.93(4)−1.93(3)−2.12(3)	1.91(2)−1.92(2)−1.92(2)−2.17(3)

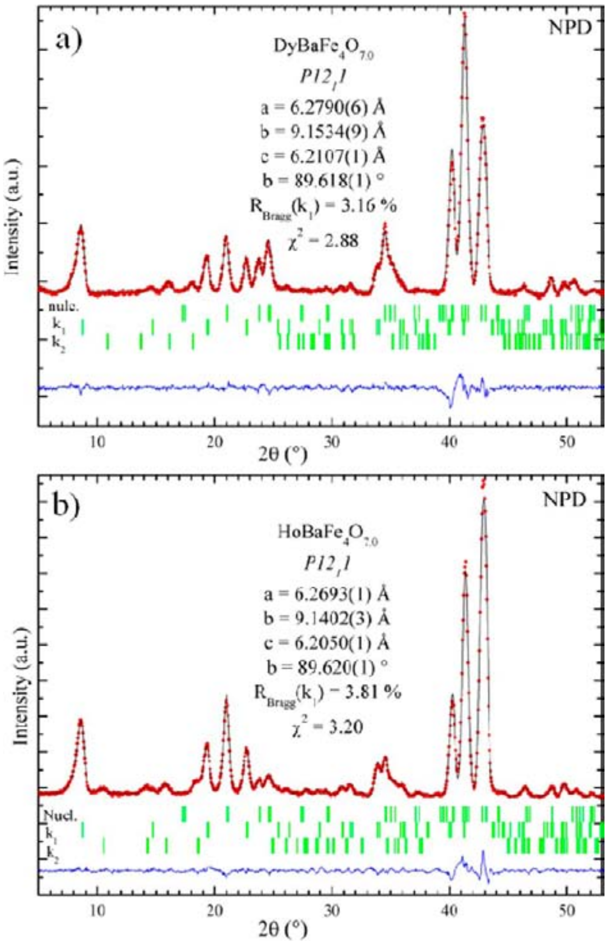

Figure 8. Rietveld nuclear and magnetic ($\mathbf{k}_1$ only) refinement of 4 K neutron patterns of (a) $DyBaFe_4O_{7.0}$ and (b) $HoBaFe_4O_{7.0}$.

weak to be investigated; these reflections were taken into account only through a LeBail fitting procedure.

Rietveld refinement of the magnetic structure associated with propagation vector $\mathbf{k}_1$ leads to a model very comparable to the magnetic structure of $YBaFe_4O_{7.0}$[24] (see this reference for a more detailed description of the magnetic structure). The magnetic moments of Fe1, Fe2, and Fe3 were strained along the $\vec{b}$ axis of the monoclinic cell, whereas the Fe4 moment was left free. For both oxides, Ln = Dy and Ho, the m_z component of Fe4 was fixed to zero in the final refinement, due to the very weak refined values obtained with low accuracy. The values of the magnetic moments (Table 6) show that the magnetic structures of these oxides, described in terms of corner-shared Fe_4 tetrahedra (Figure 9), change only slightly with the nature of Ln. The magnetic moment of Fe2 is significantly larger than those of Fe1, Fe3, and Fe4, by more than $1\mu_B$. Its value of $\sim 4\mu_B$, even larger than that of the Y-phase ($\sim 3\mu_B$), is equal to the maximum value of Fe^{2+} in a high-spin tetrahedral environment ($S = 2$). However, bearing in mind that these oxides are strongly magnetically frustrated, an important part of the magnetic moment is expected to be fluctuating, leading to values lower than those expected. This suggests that the Fe2 site is occupied not by Fe^{2+} but most probably by Fe^{3+}. The lower magnetic moments of Fe1, Fe3, and Fe4, the magnitudes of which are rather equivalent (Table 6), suggest that these three sites are preferentially occupied by Fe^{2+}. This statement is in agreement with the chemical formula $YBaFe^{3+}Fe_3{}^{2+}O_{7.0}$, which exhibits a Fe^{2+}/Fe^{3+} molar ratio equal to 3. However, Mössbauer spectroscopy measurements[24] on $YBaFe_4O_{7.0}$ have shown that the electronic configuration of these oxides could be more complex than a full charge ordering.

Centered Monoclinic Structure of $YbBaFe_4O_{7.0}$. The NPD pattern of this phase registered at 110 K (Figure 10) shows a slight distortion with respect to the tetragonal cell, but the superstructure peaks observed for Ln = Dy and Ho are not observed, suggesting that the propagation vector associated with the structural transition from tetragonal to monoclinic is for this oxide $\mathbf{k} = (0, 0, 0)$. This pattern can be indexed in the monoclinic space group C2, but in order to keep the structural filiation with the tetragonal form, the unconventional *I*121 space group has been used for the structure determination. The cell parameters at 110 K are $a = 6.2371(4)$ Å, $b = 9.0109(4)$ Å, $c = 6.2303(4)$ Å, and $\beta = 89.738(3)°$. The amplitude of the monoclinic distortion is thus much smaller than that observed for the oxides with Ln = Y, Dy, and Ho. In addition, no magnetic reflections are seen on the NPD pattern at temperature as low as 4 K, highlighting the fact that the monoclinic distortion in $YbBaFe_4O_{7.0}$ is different from that observed in $LnBaFe_4O_{7.0}$ for Ln = Y, Dy, and Ho.

The atomic coordinates (Table A4 in the Appendix) of monoclinic $YbBaFe_4O_{7.0}$ show that its structure (Figure 11) is practically identical to that of the tetragonal form described above, due to the tiny distortion of the cell. The atomic displacements corresponding to the tetragonal−monoclinic transition, indicated by arrows in Figure 11, show that the barium cations and the O1 atoms of the YbO_6 octahedra are brought closer together and that a slight tendency of the iron cations to form "Fe_2" pairs appears along $\vec{a}$ and $\vec{c}$.

The interatomic distances (Table 7) are very close to those obtained for the tetragonal form (Table 3). Two out of four Ba−O distances of 2.798 Å in the tetragonal phase are contracted to 2.71 Å in the monoclinic form, whereas the two others increase from 2.798 to 2.84 Å. The distortion mode of the YbO_6 octahedron is modified, changing from one elongated octahedron along $\vec{c}$ in the tetragonal phase to a "3 + 3" coordination with three shorter Yb−O bonds (∼2.20 Å) and three longer ones (∼2.24 Å) in the monoclinic form. The unique iron site of the tetragonal structure is split into two independent sites in the monoclinic cell, and the

Table 6. Directions and Magnitudes of Magnetic Moments at 4 K of $DyBaFe_4O_{7.0}$ and $HoBaFe_4O_{7.0}$

$DyBaFe_4O_{7.0}$					$HoBaFe_4O_{7.0}$				
site	m_x	m_y	m_z	m_{tot}	site	m_x	m_y	m_z	m_{tot}
Fe1	0	2.7(2)	0	2.7	Fe1	0	2.8(1)	0	2.8
Fe2	0	4.1(2)	0	4.1	Fe2	0	4.0(1)	0	4.0
Fe3	0	−2.1(1)	0	2.1	Fe3	0	−2.6(1)	0	2.6
Fe4	2.2(2)	1.0(4)	0	2.4	Fe4	2.4(1)	0.3(2)	0	2.4

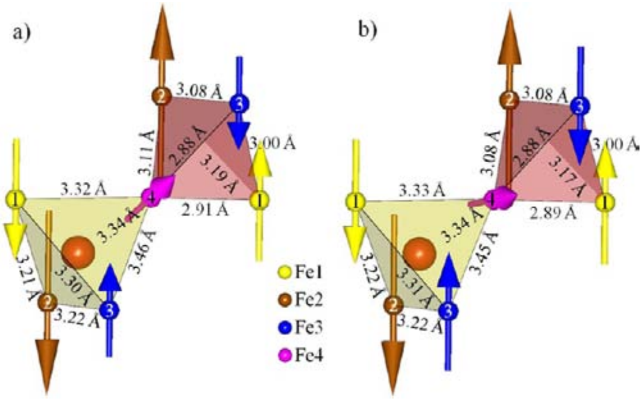

Figure 9. Detail of spin arrangement of the magnetic structure associated with propagation vector $\mathbf{k}_1$ in (a) $DyBaFe_4O_{7.0}$ and (b) $HoBaFe_4O_{7.0}$.

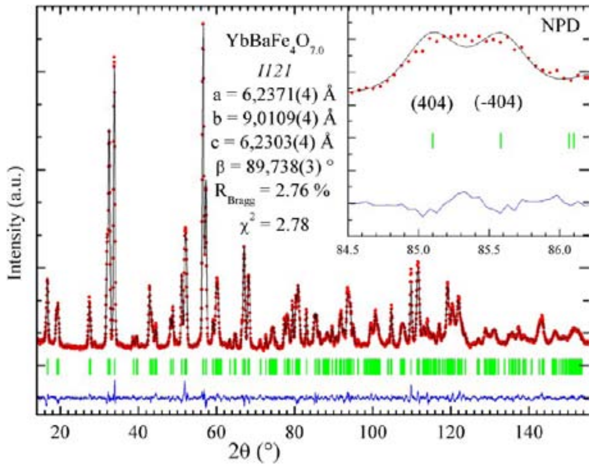

Figure 10. Rietveld refinement of neutron pattern of $YbBaFe_4O_{7.0}$ at 110 K. (Inset) Splitting of the (440) tetragonal reflection into (404) and (−404).

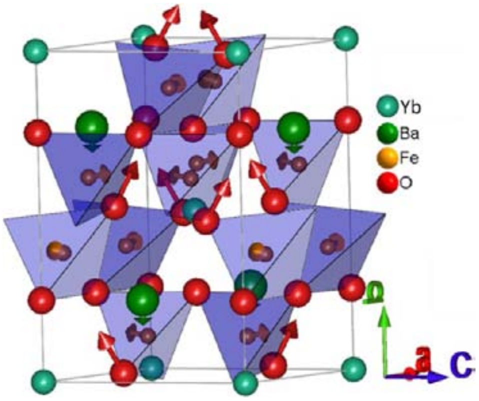

Figure 11. Atomic shifts due to the tiny monoclinic distortion of $YbBaFe_4O_{7.0}$ at 110 K.

Table 7. Interatomic Distances in Monoclinic Structure of $YbBaFe_4O_{7.0}$ at 110 K

	110 K
Ln−O (Å)	2.19(1) × 2−2.20(1) × 1
	2.23(1) × 2−2.24(1) × 1
Ba−O (Å)	2.71(3) × 2−3.119(1) × 2
	2.84(3) × 2−3.115(1) × 2
Fe1−O (Å)	1.96(2) × 1−1.89(1) × 1
	1.92(2) × 1−2.113(6) × 1
Fe2−O (Å)	1.95(2) × 1−1.94(1) × 1
	1.90(2) × 1−1.992(6) × 1

Table 8. Details of Rietveld Refinement of Tetragonal Patterns of $LnBaFe_4O_{7.0}$ (Ln = Er and Lu) at 110 and 4 K

	$ErBaFe_4O_{7.0}$[a]		$LuBaFe_4O_{7.0}$[b]	
	110 K	4 K	110 K	4 K
χ^2 (SXPD)			2.76	2.08
R_{Bragg} (SXPD)			2.6	3.33
χ^2 (NPD)	1.91	1.83	2.55	2.48
R_{Bragg} (NPD)	2.16	2.15	1.9	1.85
a_{quad} (Å)	6.2411(1)	6.2368(1)	6.2297(3)	6.2247(3)
c_{quad} (Å)	9.07478(2)	9.0768(2)	8.9923(6)	8.9990(6)
amplitude GM1 (Å)	0.522(8)	0.527(8)	0.555(6)	0.555(6)
amplitude GM5 (Å)	0.899(8)	0.915(8)	0.780(8)	0.791(8)
BVS (Ln)	3.38	3.37	3.59	3.58
BVS (Ba)	1.54	1.57	1.44	1.46
BVS (Fe)	2.19	2.2	2.25	2.26

[a] Neutron diffraction. [b] Synchrotron radiation.

Fe−O distances show that one site (Fe1) is significantly more distorted than the other one (Fe2).

Finally, it is worth pointing out that this particular structural transition to a different monoclinic symmetry for Ln = Yb, compared to the three other phases with Ln = Dy, Ho, and Y, cannot be explained by a size effect of the Ln^{3+} cation alone, since the oxides corresponding to Er^{3+} and Lu^{3+}, which are respectively larger and smaller than Yb^{3+}, remain tetragonal whatever the temperature. An electronic transfer, according to the equilibrium $Fe^{2+} + Yb^{3+} = Fe^{(2+\delta)} + Yb^{(3-\delta)+}$, may be at the origin of this particular behavior of ytterbium, in agreement with the ability of this element to be stabilized in the divalent state.

Tetragonal Structures of $LuBaFe_4O_{7.0}$ and $ErBaFe_4O_{7.0}$ at 4 K. As previously stated, the oxides $LnBaFe_4O_{7.0}$ with Ln = Er and Lu keep their tetragonal ($I\bar{4}$) symmetry from room temperature to 4 K. The structure evolves slightly with temperature; the tetragonal distortion increases with decreasing temperatures (Table 8). It is interesting to note that the anisotropic thermal displacements of the oxygen atoms coordinated to the barium (O1 and O1_2) remain similar in shape and direction up to 4 K (Table A5 in the Appendix). However, the amplitude of the displacements decreases with temperature. This behavior is the one expected for thermal factors,

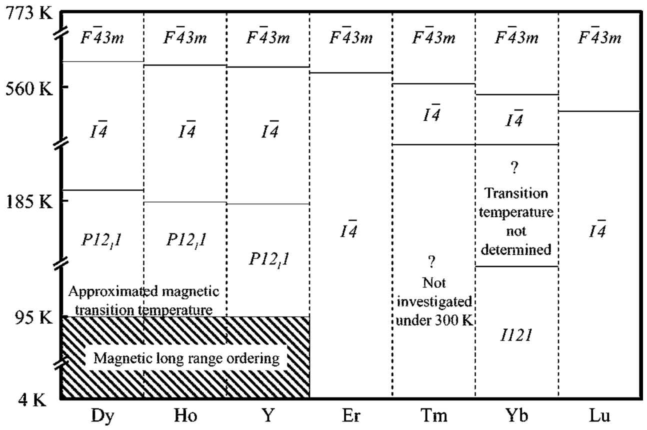

Figure 12. Phase diagram of cubic-based 114 iron oxides $LnBaFe_4O_{7.0}$ (Ln = Y and Dy to Lu).

confirming that the anisotropic atomic displacement parameters are not incorrectly used to model configuration disorder.

Finally, the NPD patterns of these two oxides do not exhibit magnetic reflections at 4 K, similar to $YBaFe_4O_7$. The absence of magnetic ordering in these oxides for Ln = Yb, Er, and Lu strongly suggests that the distortion of their tetrahedral [Fe4] framework is too weak to lift the geometrical frustration corresponding to the original cubic symmetry. This behavior is remarkably different from other oxides of the series, Ln = Y, Dy, and Ho, where the strong monoclinic distortion ($P12_11$) of the tetragonal cell ($I\bar{4}$) is at the origin of the long-range magnetic ordering. In the latter, the [Fe4] sublattice is indeed strongly distorted, so that the geometric frustration is partly lifted.

CONCLUSION

This study shows that synthesis of the series of "114" $LnBaFe_4O_{7.0}$ oxides with Ln = Dy to Lu, as for $YBaFe_4O_{7.0}$, requires drastic conditions against oxidation, even at room temperature, to preserve the "O_7" stoichiometry, in contrast to $LnBaCo_4O_7$ oxides. Though both series of cobalt and iron "114" oxides exhibit closely related structures, they differ by their symmetry, which is based on hexagonal and cubic cells, respectively. However the structural and magnetic evolution versus temperature of the "114" $LnBaFe_4O_{7.0}$ oxides, summarized in Figure 12, is similar to that of the $LnBaCo_4O_7$ oxides. One indeed observes transitions from a high-temperature form to low-temperature distortions. The reason for these structural transitions has been identified as the large underbonding of the barium cation in both Fe- and Co-based oxides.

The low-temperature magnetic behavior is also similar in the two series, since the cobaltites as well as the ferrites exhibit long-range ordering of the spins of transition elements for the larger lanthanide ions. In the case of Fe "114", the magnetic phase is clearly correlated with the existence of the monoclinic ($P12_11$) cell, and only the oxides $LnBaFe_4O_{7.0}$ with Ln = Y, Dy, and Ho exhibit magnetic long-range order. In Co"114" oxides, $LuBaCo_4O_7$ is the only one that does not exhibit long-range magnetic ordering.

Finally, it is quite remarkable that, whatever the symmetry and the nature of the transition element, cobalt or iron, the crystal chemistry of all these "114" oxides is marked by a significant underbonding of barium. We believe that this phenomenon plays a crucial role in the appearance of structural distortions and consequently influences the magnetic properties of these oxides.

APPENDIX

Table A1. Atomic Positions in Tetragonal Structures of $LnBaFe_4O_{7.0}$ at 300 K

		$DyBaFe_4O_{7.0}$[a]			$HoBaFe_4O_{7.0}$[a]		
atom	Wyck	*x*	*y*	*z*	*x*	*y*	*z*
Dy/Ho	2a	0	0	0	0	0	0
Ba	2d	0	0.5	0.75	0	0.5	0.75
Fe	8g	0.0193(6)	0.7581(6)	0.3790(3)	0.0182(6)	0.7595(6)	0.3797(2)
O1	8g	0.706(2)	0.794(2)	0.023(2)	0.7081(9)	0.7942(9)	0.0224(6)
O1_2	4e	0	0	0.7501(6)	0	0	0.7512(6)
O2	4c	0	0.5	0.25	0	0.5	0.25
		$ErBaFe_4O_{7.0}$[b]			$TmBaFe_4O_{7.0}$[c]		
atom	Wyck	*x*	*y*	*z*	*x*	*y*	*z*
Er/Tm	2a	0	0	0	0	0	0
Ba	2d	0	0.5	0.75	0	0.5	0.75
Fe	8g	0.0163(4)	0.7607(4)	0.3803(3)	−0.015(5)	0.765(2)	0.383(2)
O1	8g	0.7106(6)	0.7932(6)	0.0205(4)	0.707(5)	0.783(5)	0.032(5)
O1_2	4e	0	0	0.7519(3)	0	0	0.745(3)
O2	4c	0	0.5	0.25	0	0.5	0.25
		$YbBaFe_4O_{7.0}$[b]			$LuBaFe_4O_{7.0}$[a]		
atom	Wyck	*x*	*y*	*z*	*x*	*y*	*z*
Yb/Lu	2a	0	0	0	0	0	0
Ba	2d	0	0.5	0.75	0	0.5	0.75
Fe	8g	0.0150(6)	0.7614(4)	0.3807(2)	0.0137(4)	0.758(2)	0.3790(6)
O1	8g	0.7145(6)	0.7919(6)	0.0193(4)	0.7183(4)	0.794(4)	0.023(4)
O1_2	4e	0	0	0.7539(3)	0	0	0.750(2)
O2	4c	0	0.5	0.25	0	0.5	0.25

[a] Synchrotron radiation. [b] Neutron diffraction. [c] Thermodiffraction.

Table A2. Anisotropic Thermal Parameters of $LnBaFe_4O_{7.0}$ (Ln = Dy to Lu) at 300 K[a]

atom	U_{11} (Å^2)	U_{22} (Å^2)	U_{33} (Å^2)	U_{12} (Å^2)	U_{13} (Å^2)	U_{23} (Å^2)
$DyBaFe_4O_{7.0}$						
Dy	0.0065(6)	0.0065(6)	0.0049(9)	0	0	0
Ba	0.018(2)	0.018(2)	0.011(2)	0	0	0
Fe	0.012(2)	0.020(2)	0.016(2)	−0.001(2)	−0.001(2)	0.0096(9)
O1	0.010(4)	0.024(2)	0.021(3)	−0.0077(5)	−0.006(3)	0.012(2)
O1_2	0.0138(6)	0.055(4)	0.012(5)	0.01(2)	0	0
O2	0.021(2)	0.021(2)	0.012(9)	0	0	0
$HoBaFe_4O_{7.0}$						
Ho	0.0067(6)	0.0067(6)	0.0061(9)	0	0	0
Ba	0.018(2)	0.018(2)	0.014(2)	0	0	0
Fe	0.014(2)	0.020(2)	0.0178(9)	−0.001(2)	0.001(2)	0.0094(9)
O1	0.013(4)	0.022(4)	0.023(4)	−0.007(3)	−0.005(3)	0.013(3)
O1_2	0.014(4)	0.058(6)	0.009(4)	0.00(2)	0	0
O2	0.022(4)	0.022(4)	0.013(6)	0	0	0
$ErBaFe_4O_{7.0}$						
Er	0.013(2)	0.013(2)	0.009(3)	0	0	0
Ba	0.018(3)	0.018(3)	0.019(4)	0	0	0
Fe	0.016(1)	0.027(2)	0.022(1)	0.001(2)	−0.001(2)	0.010(2)
O1	0.014(2)	0.021(2)	0.030(2)	−0.005(2)	−0.003(2)	0.009(2)
O1_2	0.022(3)	0.050(4)	0.013(3)	0.00(1)	0	0
O2	0.027(3)	0.027(3)	0.021(4)	0	0	0
$YbBaFe_4O_{7.0}$						
Yb	0.011(1)	0.011(1)	0.007(2)	0	0	0
Ba	0.016(4)	0.016(4)	0.022(4)	0	0	0
Fe	0.012(1)	0.026(2)	0.021(1)	0.001(2)	−0.002(2)	0.011(1)
O1	0.011(2)	0.023(2)	0.034(3)	−0.005(3)	−0.001(2)	0.015(2)
O1_2	0.022(3)	0.052(4)	0.013(3)	−0.01(1)	0	0
O2	0.027(3)	0.027(3)	0.018(3)	0	0	0
$LuBaFe_4O_{7.0}$						
Lu	0.009(2)	0.009(2)	0.004(2)	0	0	0
Ba	0.015(3)	0.015(3)	0.027(4)	0	0	0
Fe	0.013(1)	0.025(2)	0.0207(8)	0.001(2)	−0.000(2)	0.012(1)
O1	0.013(2)	0.024(2)	0.037(2)	−0.009(2)	−0.008(2)	0.018(2)
O1_2	0.016(2)	0.058(4)	0.014(2)	0.00(2)	0	0
O2	0.021(2)	0.021(2)	0.015(3)	0	0	0

[a] The structure of $TmBaFe_4O_{7.0}$ was not investigated, due to the high cost of this compound.

Table A3. Atomic Positions in Monoclinic Form of $LnBaFe_4O_{7.0}$ (Ln = Dy and Ho) at 110 K

	$DyBaFe_4O_{7.0}$				$HoBaFe_4O_{7.0}$			
atom[a]	*x*	*y*	*z*	b_{iso} (Å^2)	*x*	*y*	*z*	b_{iso} (Å^2)
Dy/Ho	0.751(2)	0.75	0.257(2)	0.36(6)	0.750(2)	0.75	0.257(2)	0.36(6)
Ba	0.729(3)	0.5	0.753(3)	0.5(1)	0.732(2)	0.5	0.751(2)	0.6(2)
Fe1	0.737(3)	0.131(3)	0.001(3)	0.8(2)	0.737(2)	0.132(2)	0.003(2)	0.5(2)
Fe2	0.492(3)	0.379(3)	0.266(3)	0.8(2)	0.494(2)	0.379(2)	0.270(2)	0.6(2)
Fe3	0.983(3)	0.371(3)	0.229(3)	1.5(3)	0.982(2)	0.368(2)	0.231(2)	1.2(3)
Fe4	0.774(3)	0.140(3)	0.471(3)	1.0(3)	0.775(2)	0.139(2)	0.470(2)	1.0(3)
O1	0.741(6)	0.498(4)	0.226(6)	2.3(6)	0.742(3)	0.505(3)	0.232(3)	1.4(3)
O2	0.732(6)	−0.002(4)	0.245(6)	0.9(3)	0.732(3)	0.000(3)	0.242(3)	0.7(3)
O3	0.546(6)	0.271(5)	0.531(6)	0.7(6)	0.543(3)	0.268(3)	0.532(3)	0.1(3)
O4	0.957(6)	0.280(5)	−0.058(6)	0.9(6)	0.958(3)	0.283(3)	−0.062(3)	0.8(3)
O5	0.060(5)	0.215(5)	0.452(5)	1.1(6)	0.057(3)	0.218(3)	0.448(3)	0.2(4)
O6	0.465(6)	0.236(5)	0.048(5)	0.9(6)	0.456(3)	0.232(3)	0.039(3)	1.0(6)
O3	0.755(6)	0.013(3)	0.756(6)	2.0(5)	0.758(3)	0.005(3)	0.758(6)	1.5(4)

[a] Wyck = 2a for all atoms.

Table A4. Atomic Positions in Monoclinic Structure of $YbBaFe_4O_{7.0}$ at 110 K[a]

atom	Wyck	x	y	z	b_{iso}
Yb	2a	0	0	0	0.6(2)
Ba	2b	0.5	0.749(6)	0	0.5(3)
Fe1	4c	−0.227(2)	0.388(9)	−0.988(2)	1.3(2)
Fe2	4c	−0.015(2)	0.620(9)	−0.241(2)	0.9(2)
O1	4c	−0.203(3)	0.028(4)	−0.283(3)	0.9(3)
O2	4c	0.286(3)	0.985(4)	−0.214(4)	1.5(3)
O3	2a	0	0.756(2)	0	1.6(6)
O4	2a	0	0.249(2)	0	1.4(6)
O5	2b	0.5	0.25	0	1.9(3)

[a] a = 6.2371(4) Å, b = 9.0109(4) Å, c = 6.2303(4) Å, β = 89.738(3)°, R_{Bragg} = 2.76, χ^2 = 2.78.

Table A5. Anisotropic Thermal Parameters of $LnBaFe_4O_{7.0}$ (Ln = Er and Lu) at 4 K

atom	U_{11} (Å^2)	U_{22} (Å^2)	U_{33} (Å^2)	U_{12} (Å^2)	U_{13} (Å^2)	U_{23} (Å^2)
$ErBaFe_4O_{7.0}$						
Er	0.010(2)	0.010(2)	0.004(2)	0	0	0
Ba	0.014(3)	0.014(3)	0.012(4)	0	0	0
Fe	0.012(1)	0.025(2)	0.026(2)	0.004(2)	0.001(2)	0.020(1)
O1	0.009(2)	0.022(2)	0.023(2)	−0.003(2)	−0.002(2)	0.013(2)
O1_2	0.017(3)	0.047(4)	0.007(3)	−0.01(6)	0	0
O2	0.023(3)	0.023(3)	0.021(4)	0	0	0
$LuBaFe_4O_{7.0}$						
Lu	0.0028(4)	0.0028(4)	0.0001(6)	0	0	0
Ba	0.0077(8)	0.0077(8)	0.014(3)	0	0	0
Fe	0.0063(8)	0.021(1)	0.0201(8)	0.000(2)	−0.000(2)	0.0165(8)
O1	0.009(2)	0.023(3)	0.028(3)	−0.007(2)	−0.006(2)	0.017(2)
O1_2	0.010(2)	0.048(4)	0.010(3)	−0.006(8)	0	0
O2	0.014(2)	0.014(2)	0.014(3)	0	0	0

■ AUTHOR INFORMATION

Corresponding Author

*E-mail: vincent.caignaert@ensicaen.fr.

Notes

The authors declare no competing financial interest.

■ REFERENCES

(1) Valldor, M. *Solid State Sci.* **2004**, *6*, 251−266.
(2) Valldor, M.; Andersson, M. *Solid State Sci.* **2002**, *4*, 923−931.
(3) Huq, A.; Mitchell, J. F.; Zheng, H.; Chapon, L. C.; Radaelli, P. G.; Knight, K. S.; Stephens, P. W. *J. Solid State Chem.* **2006**, *179*, 1136−1145.
(4) Chapon, L.; Radaelli, P.; Zheng, H.; Mitchell, J. *Phys. Rev. B* **2006**, *74*, No. 172401.
(5) Caignaert, V.; Maignan, A.; Pralong, V.; Hébert, S.; Pelloquin, D. *Solid State Sci.* **2006**, *8*, 1160−1163.
(6) Soda, M.; Yasui, Y.; Moyoshi, T.; Sato, M.; Igawa, N.; Kakurai, K. *J. Magn. Magn. Mater.* **2007**, *310*, e441−e442.
(7) Markina, M.; Vasiliev, A. N.; Nakayama, N.; Mizota, T.; Yeda, Y. *J. Magn. Magn. Mater.* **2010**, *322*, 1249−1250.
(8) Khalyavin, D. D.; Chapon, L. C.; Radaelli, P. G.; Zheng, H.; Mitchell, J. F. *Phys. Rev. B* **2009**, *80*, No. 144107.
(9) Nakayama, N.; Mizota, T.; Ueda, Y.; Sokolov, A. N.; Vasiliev, A. N. *J. Magn. Magn. Mater.* **2006**, *300*, 98−100.
(10) Caignaert, V.; Pralong, V.; Hardy, V.; Ritter, C.; Raveau, B. *Phys. Rev. B* **2010**, *81*, No. 094417.
(11) Caignaert, V.; Pralong, V.; Maignan, A.; Raveau, B. *Solid State Commun.* **2009**, *149*, 453−455.
(12) Caignaert, V.; Mitchell, J. F.; ChaponL. C. 2013.
(13) Avci, S.; Chmaissem, O.; Zheng, H.; Huq, A.; Khalyavin, D. D.; Stephens, P. W.; Suchomel, M. R.; Manuel, P.; Mitchell, J. F. *Phys. Rev. B* **2012**, *85*, No. 094414.
(14) Rykov, A. I.; Ueda, Y.; Isobe, M.; Nakayama, N.; Yu, T. P.; Petrov, S. A.; Shmakov, A. N.; Kriventsov, V. N.; Vasiliev, A. N. *New J. Phys.* **2010**, *12*, No. 043035.
(15) Maignan, A.; Caignaert, V.; Pelloquin, D.; Hébert, S.; Pralong, V.; Hejtmanek, J.; Khomskii, D. *Phys. Rev. B* **2006**, *74*, No. 165110.
(16) Tsipis, E. V.; Kharton, V. V.; Frade, J. R.; Núñez, P. *J. Solid State Electrochem.* **2005**, *9*, 547−557.
(17) Kadota, S.; Karppinen, M.; Motohashi, T.; Yamauchi, H. *Chem. Mater.* **2008**, *20*, 6378−6381.
(18) Chmaissem, O.; Zheng, H.; Huq, A.; Stephens, P. W.; Mitchell, J. F. *J. Solid State Chem.* **2008**, *181*, 664−672.
(19) Pralong, V.; Caignaert, V.; Sarkar, T.; Lebedev, O. I.; Duffort, V.; Raveau, B. *J. Solid State Chem.* **2011**, *184*, 2588−2594.
(20) Caignaert, V.; Abakumov, A. M.; Pelloquin, D.; Pralong, V.; Maignan, A.; Van Tendeloo, G.; Raveau, B. *Chem. Mater.* **2009**, *21*, 1116−1122.
(21) Pralong, V.; Caignaert, V.; Maignan, A.; Raveau, B. *J. Mater. Chem.* **2009**, *19*, 8335.
(22) Raveau, B.; Caignaert, V.; Pralong, V.; Pelloquin, D.; Maignan, A. *Chem. Mater.* **2008**, *20*, 6295−6297.
(23) Duffort, V.; Caignaert, V.; Pralong, V.; Barrier, N.; Raveau, B.; Avdeev, M.; Zheng, H.; Mitchell, J. F. *J. Solid State Chem.* **2012**, *191*, 225−231.
(24) Duffort, V.; Sarkar, T.; Caignaert, V.; Pralong, V.; Raveau, B.; Avdeev, M.; Cervellino, A.; Waerenborgh, J. C.; Tsipis, E. V. *J. Solid State Chem.* **2013**, (accepted for publication).
(25) Brown, I. D.; Altermatt, D. *Acta Crystallogr., Sect. B* **1985**, *41*, 244−247.
(26) Brown, I. D. *J. Solid State Chem.* **1991**, *90*, 155−167.
(27) Brown, I. D. *J. Solid State Chem.* **1989**, *82*, 122−131.
(28) Rodríguez-Carvajal, J. *Phys. B: Condens. Matter* **1993**, *192*, 55−69.
(29) Orobengoa, D.; Capillas, C.; Aroyo, M. I.; Manuel Perez-Mato, J. *J. Appl. Crystallogr.* **2009**, *42*, 820−833.